



Identification of 1RXS J165424.6-433758 as a Polar Cataclysmic Variable

B. O'Connor^{1,2,3,4} , J. Brink^{5,6} , D. A. H. Buckley^{5,6,7,8} , K. Mukai^{9,10} , C. Kouveliotou^{1,2} , E. Göğüş¹¹ , S. B. Potter^{6,12} , P. Woudt⁵ , A. Lien¹³ , A. Levan¹⁴ , O. Kargaltsev^{1,2} , M. G. Baring¹⁵ , E. Bellm¹⁶ , S. B. Cenko^{4,17} , P. A. Evans¹⁸ , J. Granot^{1,19,20} , C. Hailey²¹ , F. Harrison²² , D. Hartmann²³ , A. J. van der Horst^{1,2} , D. Huppenkothen²⁴ , L. Kaper²⁵ , J. A. Kennea²⁶ , P. O. Slane²⁷ , D. Stern²⁸ , E. Troja²⁹ , R. A. M. J. Wijers^{1,30} , and G. Younes^{1,2}

¹ Department of Physics, The George Washington University, Washington, DC 20052, USA; oonorb@gwmail.gwu.edu

² Astronomy, Physics and Statistics Institute of Sciences (APSiS), The George Washington University, Washington, DC 20052, USA

³ Department of Astronomy, University of Maryland, College Park, MD 20742-4111, USA

⁴ Astrophysics Science Division, NASA Goddard Space Flight Center, 8800 Greenbelt Rd., Greenbelt, MD 20771, USA

⁵ Department of Astronomy, University of Cape Town, Private Bag X3, Rondebosch 7701, South Africa

⁶ South African Astronomical Observatory, P.O. Box 9, Observatory 7935, Cape Town, South Africa

⁷ Southern African Large Telescope, P.O. Box 9, Observatory 7935, Cape Town, South Africa

⁸ Department of Physics, University of the Free State, P.O. Box 339, Bloemfontein 9300, South Africa

⁹ CRESST II and X-ray Astrophysics Laboratory, NASA/GSFC, Greenbelt, MD 20771, USA

¹⁰ Department of Physics, University of Maryland Baltimore County, 1000 Hilltop Circle, Baltimore, MD 21250, USA

¹¹ Sabancı University, Faculty of Engineering and Natural Sciences, Istanbul 34956, Turkey

¹² Department of Physics, University of Johannesburg, PO Box 524, Auckland Park 2006, Johannesburg, South Africa

¹³ University of Tampa, Department of Chemistry, Biochemistry, and Physics, 401 W. Kennedy Blvd., Tampa, FL 33606, USA

¹⁴ Department of Astrophysics/IMAPP, Radboud University, P.O. Box 9010, 6500 GL, The Netherlands

¹⁵ Department of Physics and Astronomy—MS 108, Rice University, 6100 Main St., Houston, TX 77251-1892, USA

¹⁶ DIRAC Institute, Department of Astronomy, University of Washington, 3910 15th Ave. NE, Seattle, WA 98195, USA

¹⁷ Joint Space-Science Institute, University of Maryland, College Park, MD 20742 USA

¹⁸ School of Physics and Astronomy, University of Leicester, University Rd., Leicester, LE1 7RH, UK

¹⁹ Department of Natural Sciences, The Open University of Israel, P.O. Box 808, Ra'anana 43537, Israel

²⁰ Astrophysics Research Center of the Open University (ARCO), The Open University of Israel, P.O. Box 808, Ra'anana 43537, Israel

²¹ Columbia Astrophysics Laboratory, Columbia University, New York, NY 10027, USA

²² Cahill Center for Astrophysics, California Institute of Technology, 1216 East California Blvd., Pasadena, CA 91125, USA

²³ Department of Physics and Astronomy, Clemson University, Kinard Lab of Physics, Clemson, SC 29634-0978, USA

²⁴ SRON Netherlands Institute for Space Research, Niels Bohrweg 4, 2333CA Leiden, The Netherlands

²⁵ University of Amsterdam, Science Park 904, 1098 XH Amsterdam, The Netherlands

²⁶ Department of Astronomy and Astrophysics, The Pennsylvania State University, 525 Davey Lab, University Park, PA 16802, USA

²⁷ Center for Astrophysics, Harvard & Smithsonian, 60 Garden St., Cambridge, MA 02138, USA

²⁸ Jet Propulsion Laboratory, California Institute of Technology, 4800 Oak Grove Dr., Mail Stop 169-221, Pasadena, CA 91109, USA

²⁹ University of Rome Tor Vergata, Department of Physics, via della Ricerca Scientifica 1, I-00100, Rome, IT, Italy

³⁰ Anton Pannekoek Institute, University of Amsterdam, Postbus 94249, 1090 GE Amsterdam, The Netherlands

Received 2023 June 8; revised 2023 August 24; accepted 2023 September 8; published 2023 November 2

Abstract

We present the results of our X-ray, ultraviolet, and optical follow-up campaigns of 1RXS J165424.6-433758, an X-ray source detected with the Swift Deep Galactic Plane Survey. The source X-ray spectrum (Swift and NuSTAR) is described by thermal bremsstrahlung radiation with a temperature of $kT = 10.1 \pm 1.2$ keV, yielding an X-ray (0.3–10 keV) luminosity $L_X = (6.5 \pm 0.8) \times 10^{31}$ erg s⁻¹ at a Gaia distance of 460 pc. Spectroscopy with the Southern African Large Telescope revealed a flat continuum dominated by emission features, demonstrating an inverse Balmer decrement, the $\lambda 4640$ Bowen blend, almost a dozen He I lines, and He II $\lambda 4541$, $\lambda 4686$, and $\lambda 5411$. Our high-speed photometry demonstrates a preponderance of flickering and flaring episodes, and revealed the orbital period of the system, $P_{\text{orb}} = 2.87$ hr, which fell well within the cataclysmic variable (CV) period gap between 2 and 3 hr. These features classify 1RXS J165424.6-433758 as a nearby polar magnetic CV.

Unified Astronomy Thesaurus concepts: [AM Herculis stars \(32\)](#); [Cataclysmic variable stars \(203\)](#); [X-ray astronomy \(1810\)](#)

1. Introduction

Cataclysmic variables (CVs) are binary systems composed of a white dwarf (WD) and a late-type main-sequence star. An accretion disk will also form if the WD's magnetic field is $< 10^6$ G (Warner 1995). In systems with a highly magnetic WD ($\sim 10^{6-9}$ G) the accretion disk is either fully (Cropper 1990; e.g.,

AM Herculis, a polar CV), or partially disrupted (Patterson 1994; e.g., DQ Herculis, an intermediate polar (IP) CV).

In polar magnetic CVs (mCVs), matter from the companion star accretes onto the WD poles following the magnetic field lines. As the matter in the accretion column collides with the WD atmosphere a shock is formed, which emits cyclotron (optical/infrared (IR)) and thermal bremsstrahlung (X-rays) radiation. Polars have typical soft X-ray (0.3–10 keV) luminosities $\sim 10^{30-32}$ erg s⁻¹.

In these systems, the large magnetic field ($> 10^7$ G) causes synchronicity with the companion star, such that the orbital period and WD rotational period are the same. Angular momentum losses



Original content from this work may be used under the terms of the [Creative Commons Attribution 4.0 licence](#). Any further distribution of this work must maintain attribution to the author(s) and the title of the work, journal citation and DOI.

lead to an evolution of the orbital period over time. In CVs with large orbital periods (>3 hr), the orbit is dominated by magnetic breaking, while in short-period binaries (<2 hr) gravitational radiation losses are the dominant factor. However, magnetic breaking is thought to be ineffective when the companion star becomes fully convective, leading to the so-called “period gap” between 2 and 3 hr (Knigge 2006). Despite this, many polars are discovered with orbital periods lying in this gap, requiring new theories of mCV formation and evolution (e.g., magnetic field evolution or reduced magnetic braking; Li et al. 1994; Belloni et al. 2020; Webbink & Wickramasinghe 2002).

Disruption of the accretion disk reduces the thermal instabilities in these systems, making novae and outbursts less common than in nonmagnetic CVs. As a result, mCVs are rare in optical surveys (Oliveira et al. 2017, 2020). For example, Szkody et al. (2020) found that only $\sim 1/100$ CVs discovered in optical surveys are magnetic. However, using a volume-limited (<150 pc) sample, Pala et al. (2020) showed that 36% of CVs, selected using Gaia parallaxes, are magnetic. This emphasizes the need for X-ray surveys (e.g., eROSITA) to improve the discovery rate of mCVs (see also Bernardini et al. 2012).

In this work, we introduce the discovery of a new polar through the Swift Deep Galactic Plane Survey (DGPS; O'Connor et al. 2023a), a Swift Key Project and NuSTAR Legacy Project. The DGPS covers 40 degrees² of the Galactic plane between $10^\circ < |l| < 30^\circ$ in longitude and $|b| < 0.5^\circ$ in latitude, to luminosity $L_X > 10^{34}$ erg s⁻¹, out to 3–6 kpc. The DGPS has also revealed the discovery of a distant IP CV (Gorgone et al. 2021) and a candidate IP (O'Connor et al. 2023b), totaling three mCVs serendipitously discovered by the survey.

1RXS J165424.6-43375 (hereafter J1654) was discovered with ROSAT in 1990 August, and later with ASCA as AX J165420-4337. The Chasing the Identification of ASCA Galactic Objects (ChIcAGO) survey identified the X-ray counterpart to AX J165420-4337 using Chandra (Anderson et al. 2014). The source was later observed with Swift (Reynolds et al. 2013) as part of a shallow Galactic plane survey.

Takata et al. (2022) analyzed a sample of unclassified X-ray sources with Gaia counterparts, including J1654 (G596 in that paper). Using a combination of Swift, NuSTAR, and the Transiting Exoplanet Survey Satellite (TESS), they classify J1654 as a candidate polar. In particular, their result is due to the periodicity of 2.88 hr uncovered by TESS, and the fact that no other periodicity is identified, suggesting the spin and orbital periods may be locked. However, they do not exclude the possibility that J1654 is an IP.

Here, we present DGPS observations and follow up of J1654 obtained using our approved Target of Opportunity (ToO) programs. We obtained observations with Swift, NuSTAR, the Southern African Large Telescope (SALT), and the South African Astronomical Observatory (SAAO) 1 m telescope. We also analyze archival optical and IR observations, and archival XMM-Newton observations. We uncover clear low- and high-state transitions in the ultraviolet (UV), optical, IR, and X-rays. The low-state photometry allows us to analyze the secondary star, determining that it is likely of late spectral type. High-speed photometry carried out over multiple nights yields an orbital period of ~ 2.87 hr, in agreement with Takata et al. (2022). Our optical spectroscopy reveals numerous lines of hydrogen and helium, demonstrating an inverse Balmer decrement. In particular, our spectroscopic observations point toward the classification of the source as a typical polar at a

Gaia distance of ~ 460 pc, solidifying its previous classification (Takata et al. 2022).

We present the observations and analysis in Section 2. The results of our timing and spectroscopic analyses are presented in Section 3, with a brief discussion in Section 4 and conclusions in Section 5. Throughout the manuscript errors are quoted at the 1σ level and upper limits at the 3σ level, unless otherwise stated.

2. Observations and Data Analysis

We begin by presenting our UV, optical, and IR data analysis in Section 2.1, including optical spectroscopy (Section 2.1.3) and high-speed photometry (Section 2.1.4). This is followed by the description of our X-ray data analysis in Section 2.2.

2.1. UV, Optical, and IR Data

2.1.1. Archival Multiwavelength Data

Throughout the paper, we utilize the archival Chandra localization of J1654 at R.A., decl. (J2000) = $16^h54^m23^s.45$, $-43^\circ37'43''.8$ with an uncertainty of $0''.43$ (68% CL; Evans et al. 2010; Anderson et al. 2014). This position is covered by multiple archival surveys, including Gaia (Gaia Collaboration et al. 2016, 2018; Gaia Collaboration 2020), the VISTA Variables in the Vía Láctea (VVV) Infrared Astrometric Catalogue (VIRAC; Smith et al. 2018), the VST Photometric H α Survey of the Southern Galactic Plane and Bulge (VPHAS; Drew et al. 2014), the Asteroid Terrestrial-impact Last Alert System (ATLAS) reference catalog (Tonry et al. 2018), and the Galactic Legacy Infrared Mid-Plane Survey Extraordinaire (GLIMPSE; Benjamin et al. 2003). In these catalogs we identify a bright optical and IR counterpart coincident with the Chandra localization (Figure 1). We tabulate archival photometry from these catalogs in Table 1.

The Gaia counterpart yields a nearby distance of $d = 463 \pm 24$ pc (Bailer-Jones et al. 2021) for J1654. Moreover, the counterpart has a high proper motion of $\mu_{R.A.} = 22.2 \pm 0.3$ mas yr⁻¹ and $\mu_{decl.} = -7.3 \pm 0.3$ mas yr⁻¹. However, this proper motion is not high enough to have impacted the source's X-ray localization over the past 20 years by more than $\sim 0''.5$.

We also performed an analysis of public archival data obtained in multiple epochs. We retrieved calibrated VPHAS images from the ESO Archive Science Portal.³¹ VPHAS photometry was obtained in two epochs: 2013 July 27 in *ri*(H α) and 2015 April 23 in the *ugr* filters. We performed aperture photometry using SExtractor with an aperture radius of $1.5\times$ the image FWHM. The photometry was calibrated to VPHAS DR2 for the *ri* filters and ATLAS for the *g* filter. The photometry derived on 2013 July 27 agrees with that presented in VPHAS DR2, but on 2015 April 23 the source is brighter by ~ 2 magnitudes, which is indicative of a high-state versus low-state transition (Warner 1999; Hessman et al. 2000; Wu & Kiss 2008). The photometry is reported in Table 1.

We performed a similar analysis of the archival VVV data to search for state changes. The calibrated images were retrieved from the ESO Archive Science Portal. Observations covering the field of J1654 were obtained in the *ZYJHK* filters. The *Z*-band photometry covers five epochs, whereas *YJH* images were obtained only in two epochs on 2014 November 12 and 2017 January 18. We performed photometry using SExtractor, and determined the photometric zero-point by calibrating to point sources in the

³¹ <https://archive.eso.org/scienceportal/home>

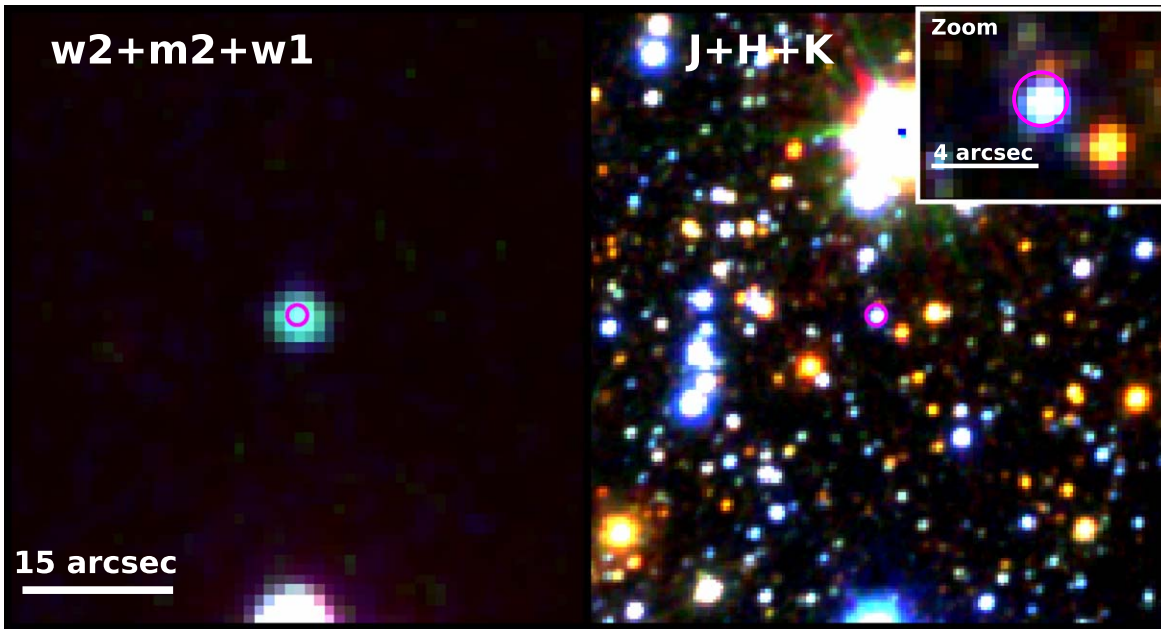


Figure 1. RGB image of the field of J1654 using three UVOT filters (left: red = $uvw1$, green = $uvm2$, and blue = $uvw2$) and three VVV filters (right: red = K_s , green = H , and blue = J). The archival Chandra localization ($1''.0$; 95% CL) is displayed by the magenta circle. In the top right a zoom in on the position of the counterpart is shown. North is up and east is to the left.

Table 1
Photometry of the Optical/IR Counterpart to J1654

Source	Filter	High State m_λ (mag)	Low State m_λ (mag)	Δm_λ
OM	$UVM2$...	>21.2	>1.3
OM	$UVW1$...	21.5 ± 0.2	2.1
OM	B	...	>20.9	...
OM	V	...	>19.4	...
UVOT	$uvw2$	19.91 ± 0.07
UVOT	$uvm2$	19.77 ± 0.11	...	>1.3
UVOT	$uvw1$	19.34 ± 0.07	...	2.1
UVOT	u	18.72 ± 0.10
Gaia	G_{BP}	18.25 ± 0.16
Gaia	G	17.83 ± 0.13
Gaia	G_{RP}	17.27 ± 0.10
ATLAS	g	18.36 ± 0.19
ATLAS	r	17.61 ± 0.14
ATLAS	i	17.26 ± 0.13
ATLAS	z	17.09 ± 0.13
VPHAS	g	18.38 ± 0.02
VPHAS	r	17.65 ± 0.02	19.94 ± 0.06	2.3
VPHAS	i	...	18.97 ± 0.03	...
VIRAC	Z	17.03 ± 0.02	18.10 ± 0.05	1.1
VIRAC	Y	16.67 ± 0.02	17.41 ± 0.03	0.7
VIRAC	J	16.45 ± 0.03	16.66 ± 0.05	0.2
VIRAC	H	16.50 ± 0.05	16.66 ± 0.08	0.16
VIRAC	K	16.80 ± 0.03	...	<0.1
GLIMPSE	$3.6 \mu\text{m}$	16.84 ± 0.13
GLIMPSE	$4.5 \mu\text{m}$	16.58 ± 0.16

Note. The magnitudes m_λ are reported in the AB magnitude system. We report photometry of the source in both the high and low states when available, as well as the difference between photometry obtained in the two states. The photometry is not corrected for interstellar reddening. Upper limits are reported at the 3σ level.

VIRAC catalog for the $ZYJH$ bands and VVV DR2 (Minniti et al. 2017) for the K band. Based on the z -band variability ($\Delta m_\lambda \sim 1.1$ mag), we find that the observations obtained on 2017 January

18 are in a high state, and those from 2014 November 12 are in a low state (see Table 1).

We further searched images obtained by the Spitzer Space Telescope (hereafter Spitzer) through GLIMPSE. Point-spread function (PSF) photometry was performed with `SEXTRACTOR`, calibrated to GLIMPSE standards in the field. The results are shown in Table 1.

2.1.2. UV Observations

Data obtained with the Swift UltraViolet and Optical Telescope (UVOT; Roming et al. 2005; Breeveld et al. 2011) were analyzed using `HEASOFT v6.29c` with `CALDB` version 20211108. The counterpart was detected in all single UVOT exposures in the $uvw2$, $uvm2$, $uvw1$, and u filters. A finding chart is shown in Figure 1. We performed aperture photometry using the `uvot-source` task with a circular source aperture of radius $5''$ and a nearby circular background region of radius $15''$. The photometry is reported in Table A2 in the AB magnitude system.

We likewise analyzed archival data obtained with the XMM-Newton Optical/UV Monitor (OM) Telescope (Mason et al. 2001). Observations were carried out in the $UVM2$, $UVW1$, B , and V filters. The source is detected ($\sim 5\sigma$) only in the $UVW1$ filter, which has the longest exposure time (5000 s). We used the `omichain` command to reduce the data. We used `omdetect` to determine the source count rates and the `ommag` task to determine the instrumental magnitudes. We converted the instrumental magnitudes to the AB system using the standard zero-points.³²

2.1.3. SALT Optical Spectroscopy

Longslit spectroscopic observations were conducted using the 10 m class SALT (Buckley et al. 2006) equipped with the Robert Stobie Spectrograph (RSS; Burgh et al. 2003; Kobulnicky et al. 2003; Smith et al. 2006). An initial spectrum

³² https://xmm-tools.cosmos.esa.int/external/xmm_user_support/documentation/uhb/omfilters.html

was obtained on 2022 April 26 using the low-resolution PG0300 grating at a grating tilt of $5^{\circ}.75$ with slit width $1''.25$. The spectrum covered the wavelength range $3200 \text{ \AA} - 9000 \text{ \AA}$ with a resolution of $R \approx 400$ at the central wavelength (6210 \AA). Additional frame-transfer spectroscopic observations were conducted on 2022 May 2, 10, and 27 using the high-resolution PG0900 grating at a grating tilt $14^{\circ}.75$ with a slit width of $1''.25$. The frame-transfer spectra covered $4060 \text{ \AA} - 7120 \text{ \AA}$ with a resolution of $R \approx 1200$ at the central wavelength (5620 \AA). The exposure time for the frame-transfer spectra is 100 s. A log of SALT observations is provided in Table A3.

The spectra were reduced using the `PySALT` package (Crawford et al. 2010), which includes bias subtraction, flat fielding, amplifier mosaicing, and a process to remove cosmetic defects. The spectra were wavelength calibrated, background subtracted, and extracted using standard IRAF³³ procedures. We obtained a relative flux calibration of all spectra using spectrophotometric standard stars. For the observation obtained on 2022 April 26, we used the standard star HILT600, and for the frame-transfer observations we used the star LTT4364. The frame-transfer observations were further continuum normalized, and used to create trailed spectra. The spectra are discussed in Section 3.4.

2.1.4. SAAO High-speed Photometry

We obtained high-speed photometry using the Sutherland High speed Optical Camera (SHOC; Coppejans et al. 2013) mounted on the SAAO 1 m telescope. Observations took place on 2022 May 4, 5, and 8 and 2022 June 1, 2, 7, and 8. The observations were performed in the *clear* and *g'r'i'* filters with exposure times of either 5 or 10 s (see Table A3). The weather was clear on all nights except 2022 May 8, and we ignore these data in the rest of our analysis.

The CCD images were reduced using the `TEA-Phot` package (Bowman & Holdsworth 2019), which was specifically designed to work with SHOC data cubes. `TEA-Phot` includes the subtraction of median-combined bias images and a median-combined flat-field correction to reduce the CCD images, and then uses a comparison star to produce a differential light curve of the target through adaptive elliptical aperture photometry. We used Two Micron All Sky Survey (2MASS) 16542993-4337457 ($J = 12.467$) as the comparison star for `TEA-Phot`. We discuss the resulting light curves in Section 3.1.

2.2. X-Ray Data

2.2.1. Swift/XRT

We retrieved the fully calibrated Swift data products from the NASA High Energy Astrophysics Science Archive Research Center (HEASARC) server. A log of the X-ray observations is given in Table A1. All observations of J1654 with the X-ray Telescope (XRT; Burrows et al. 2005) were carried out in PC mode for a total of 10.3 ks. We reduced the data using `xrtpipeline` within `HEASoft v6.29c` with `CALDB` version 20210915. We then used the `sosta` task within `ximage` to determine the source count rates, and corrected the rates for PSF losses. We extracted the source spectra from circular regions of radius 20 pixels (1 pixel = $2''.36$) and the background spectra were

extracted within a nearby region of the same size. The spectra were grouped to a minimum of 1 count bin⁻¹. Using the Swift/XRT data products generator³⁴ we derive an XRT enhanced position (Evans et al. 2009) of R.A., decl. (J2000) = $16^{\text{h}}54^{\text{m}}23^{\text{s}}.40$, $-43^{\circ}37'44''.0$ with an uncertainty of $2''.5$.

2.2.2. Swift/BAT

The source does not appear in the Swift Burst Alert Telescope (BAT; Barthelmy et al. 2005) catalogs (Krimm et al. 2013; Oh et al. 2018; Baumgartner et al. 2013). However, as a check, we reanalyzed data obtained on 2020 June 18 (ObsID: 03110780002) with an exposure of 3974 s in survey mode. We performed the standard BAT survey data analysis using the `HEASoft` tool (`CALDB` version 20171016), `batsurvey v6.16`, which reports the count rate at the source location in eight energy bands between 14 and 195 keV. The analysis does not find any significant detections. The overall signal-to-noise ratio during this period in the 14–195 keV band is ~ 0.5 , which is consistent with a background noise fluctuation.

To estimate the flux upper limit, we create a spectrum file using the count rate information, and generated the corresponding instrumental response files using the `HEASoft` tool, `batdrngen`. The upper limit was determined using `XSPEC v12.12.1` assuming a power-law model with photon index $\Gamma = 2$. Specifically, we adopted the `npepov` model, which is the model used in the BAT GRB catalogs (Sakamoto et al. 2011; Lien et al. 2016). This analysis yields a flux upper limit of $< 7.0 \times 10^{-10} \text{ erg cm}^{-2} \text{ s}^{-1}$ (90% CL) in the 14–195 keV energy range.

Furthermore, we performed a search using the BAT transient monitor (Krimm et al. 2013) pipeline and found no significant detections or outbursts (15–50 keV) from the source over the lifetime of the Swift mission ($\sim 18 \text{ yr}$).

2.2.3. NuSTAR

On 2020 August 2, we carried out a NuSTAR ToO observation of J1654 for 26 ks. We used standard tasks within the NuSTAR Data Analysis Software pipeline (`NuSTARDAS`) within `HEASoft v6.29c` with `CALDB` version 20220131 to extract light curves and spectra from a circular region of size $30''$ for both FPMA and FPMB. The source region is covered by stray light, and we carefully chose the background region ($60''$) to reflect this issue. Spectra were grouped to a minimum of 15 counts bin⁻¹. The arrival time of photons were barycenter corrected³⁵ to the solar system using the Chandra source localization (Anderson et al. 2014).

2.2.4. XMM-Newton

We analyzed an archival XMM-Newton observation covering the field of J1654 (Table A1) with a total exposure of 15 ks. The observations were performed in Full Frame mode with the medium filter. We analyze and produce separate spectra for the three XMM-Newton detectors (PN/MOS1/MOS2). The data were reduced and analyzed using tasks with the Science Analysis System (`SAS v18.0.0`) software using the latest CCF as of 2022 March. We extracted the source photons in a circular region identified by the `eregionanalyse` task. The background photons were taken from an annulus surrounding

³³ IRAF is distributed by the National Optical Astronomy Observatory, which is operated by the Association of Universities for Research in Astronomy (AURA) under cooperative agreement with the National Science Foundation (NSF).

³⁴ https://www.swift.ac.uk/user_objects/

³⁵ <https://heasarc.gsfc.nasa.gov/ftools/caldb/help/barycorr.html>

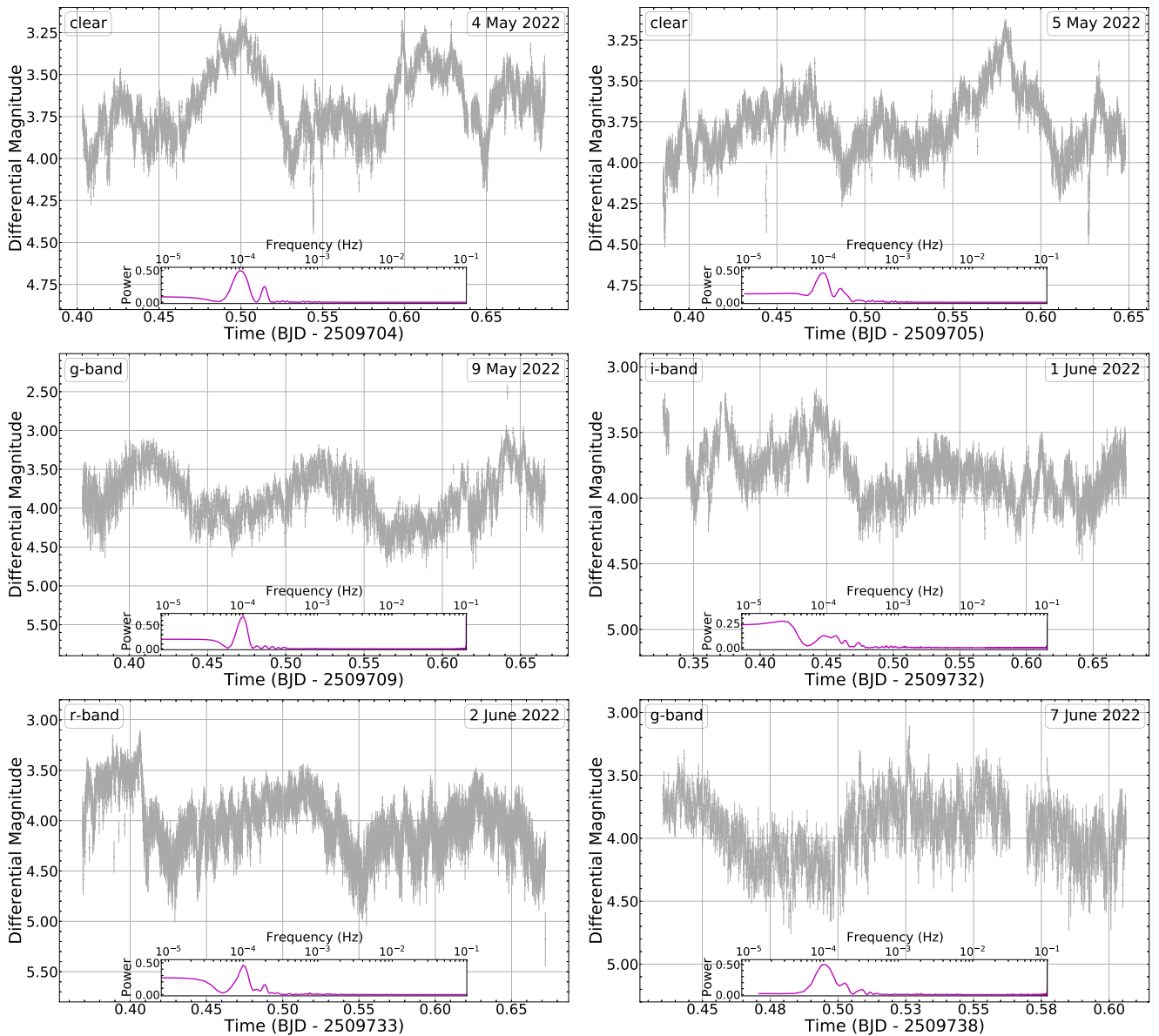


Figure 2. Optical light curves of J1654 from the 1 m SAAO telescope obtained on different nights, labeled by their barycentric Julian date (BJD). The photometry is measured as differential instrumental magnitudes, dependent on the observing conditions on each night. The inset displays the periodogram for each night.

the source with radii of $60''$ and $100''$, respectively. Spectra were grouped to a minimum of 1 count bin^{-1} . The response matrix and ancillary response files were obtained using the `rmfgen` and `arfgen` tasks, respectively. The event arrival times were barycenter corrected to the solar system using the `barycen` task. Using the PN data, we localize the source to R.A., decl. (J2000) = $16^{\text{h}}54^{\text{m}}23^{\text{s}}.43$, $-43^{\circ}37'43''.4$ with an uncertainty of $0''.65$ (68% CL; Traulsen et al. 2020), consistent with the Swift/XRT position and the archival Chandra localization.

3. Results

3.1. Optical Light Curves and Timing Analysis

Our initial high-speed photometry light curves exhibited characteristic features of polars, such as dips, flares, and flickering, with amplitudes of up to 1 mag. In order to search for an orbital period, we employed a Lomb–Scargle period search with `Gatspy`

(Vanderplas 2015) to identify significant coherent pulsations in the differential light curves produced by `TEA-Phot` (Figure 2). We built periodograms for each individual night (Figure 2) as well as a combined periodogram after normalizing the light curves to the same scale (Figure 3). We identify a significant signal at a period of 2.87 hr ($10,359 \pm 111$ s), which we interpret as the orbital period. The significance of this signal is at the $>5\sigma$ level. We also identify a harmonic of this period. No other significant lower frequency signals were identified in the periodogram at expected beat frequencies for IP systems.

We note that an independent analysis of data from TESS was carried out by Takata et al. (2022; their source G596) who find a period of 0.12 days (2.88 hr). Our observations are in agreement with their result.

3.2. X-Ray Light Curves and Timing Analysis

We compiled available archival X-ray observations of J1654 (Table A1) in order to produce a long-term X-ray light curve of

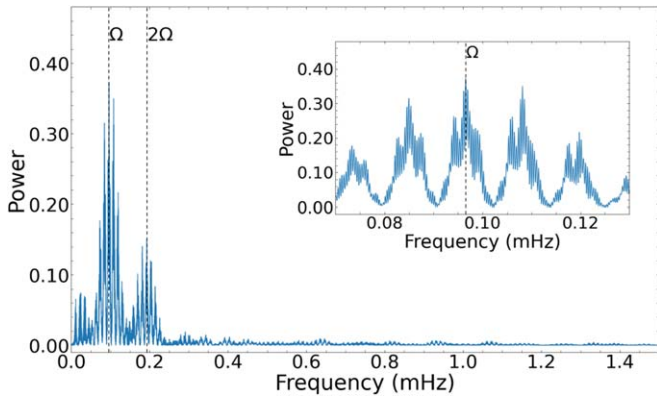


Figure 3. Lomb–Scargle periodogram of the combined optical data obtained with the SAAO. The orbital period Ω (main peak) and its harmonic are observed. The inset shows a zoom in on the frequency corresponding to the orbital period of 2.87 hr, and its aliases.

the source. We display this light curve, covering the period from 2007 to 2022, in Figure 4 (top). Based on our analysis, we identify that the XMM-Newton observation from 2012 August 20 was obtained during a low state (Warner 1999), while all other available X-ray observations, including ROSAT (1990) and ASCA, detected the source during a high state. We discuss a comparison between the NuSTAR high state and XMM-Newton low state in Section 3.4.1.

We searched the NuSTAR and XMM-Newton observations for coherent pulsations using both Z^2 statistics (Buccheri et al. 1983) and a Lomb–Scargle frequency analysis (Scargle 1982). We searched both the 3–10 keV and 3–79 keV NuSTAR light curves (Figure 4; bottom), and the 0.3–3 keV and 0.3–10 keV XMM-Newton light curves. For the NuSTAR data we searched both the FMPA and FMPB data separately, as well as the combined events file. We likewise searched both PN, MOS1, MOS2, and the combined events files for XMM-Newton for both energy ranges. No significant signal was identified in our analysis. While the NuSTAR observation does indeed cover about 5.3 orbital cycles, we did not find any significant signal at 2.87 hr in either data set, nor at any other frequency. We are able to set a 3σ upper limit to the rms pulsed fraction of $<9\%$ in the 3–79 keV energy range using the NuSTAR data (FMPA/FMPB) and $<25\%$ in the 0.3–10 keV energy range using the XMM-Newton data (PN/MOS1/MOS2).

The lack of other signals in the data besides the orbital period at 2.87 hr identified in our optical data (Section 3.1) is in agreement with the independent analysis of Takata et al. (2022). Takata et al. (2022) likewise did not identify any periods at shorter or longer values than the orbit, which would have been expected for an IP system.

3.3. Spectral Energy Distribution

We compiled all available UV, optical, and IR photometry of J1654 (Table 1) in order to build the source’s spectral energy distribution (SED). We discovered significant variability in the UV and optical filters by ~ 1 –2 mag, with the largest variability amplitude in the UV. The variability was identified as the transition between a high and low state, as shown in Figure 5. In the high state, the UV/optical emission from the accretion column dominates, but during periods of low accretion we observe the contribution of the secondary star, peaking in the near-infrared. An additional component, interpreted as cyclotron emission, is observed at longer wavelengths (3–5 μm from

Spitzer/GLIMPSE). At UV wavelengths, we begin to observe either the contribution from the WD, modeled as a simple blackbody, or emission from the accretion column that is fainter due to a lower accretion rate during those periods. Given the sparse UV data during the low state it is not possible to disentangle between those contributions. Further UV observations would be critical to constrain these possibilities.

The low-state SED is well sampled in the optical and IR (Table 1), allowing us to identify the spectral type of the secondary star. We applied the ARIADNE (Vines & Jenkins 2022) code to perform dynamic nested sampling with *dynesty* (Speagle 2020) in order to determine the best-fit secondary star parameters over a range of stellar models (e.g., Kurucz 1979; Castelli & Kurucz 2003; Husser et al. 2013). We find an effective temperature of 4700^{+800}_{-200} K, surface gravity $\log g = 4.7^{+0.6}_{-0.4}$, stellar radius $R = 0.32^{+0.07}_{-0.04} R_{\odot}$, metallicity $[\text{Fe}/\text{H}] = -0.12 \pm 0.15$, significant extinction $A_V = 4.9^{+1.1}_{-0.7}$ mag, and distance of 454 ± 20 pc, which is in good agreement with the Gaia estimate (Bailer-Jones et al. 2018, 2021). A corner plot of these results is displayed in Figure B1 and the best fit is shown in Figure 5 (blue solid line). Overall these values are consistent with a star of spectral type K3.5V.

The orbital period and $i - K$ color also favor a main-sequence donor star of late spectral type, but instead closer to spectral types between M3V and M5V (Knigge 2006). Without optical spectroscopy of the secondary star during the low state we cannot rule out other spectral types, but note the SED clearly favors a late spectral type. Moreover, using a photometric distance estimate based on the K -band apparent magnitude (Bailey 1981; Warner 1987; Knigge et al. 2011), we find a lower limit to the distance of $d \gtrsim 300$ pc, which is consistent with the Gaia result (Bailer-Jones et al. 2021). The estimate is a lower limit given that we cannot rule out an additional emission component (e.g., a circumbinary dust disk or cyclotron radiation; Brinkworth et al. 2007; Harrison & Campbell 2015), besides the secondary, contributing to the observed K -band flux.

We note that the ARIADNE model only represents one possible range of solutions. For example, the H -band photometric point (Figure 5) is underestimated in this model, though this could also be due to the source not fully being in the low state at the time of this measurement. As an additional check on the secondary star spectral type, we test whether a less-extinct M dwarf can explain the low-state SED. We performed a “by-eye” check, comparing Kurucz models (Kurucz 1979) to the SED. We find an appropriate match for an M2V dwarf at a distance of 460 pc, with temperature $T \sim 3500$ K, surface gravity $\log g \sim 4.7$, metallicity $\log Z/Z_{\odot} \sim 1$, and radius $R \sim 0.3 R_{\odot}$ (see, e.g., Parsons et al. 2018) with extinction of $A_V \sim 0.5$ mag. This model is also shown in Figure 5 (gray solid line). With the available constraints on the spectral type, we cannot exclude either of the two scenarios (e.g., K versus M dwarf), but can conclude that a late spectral type is the most likely.

In order to determine the contribution from cyclotron radiation in the IR, and in particular at Spitzer wavelengths, we applied the cyclotron models from Potter et al. (2002). These calculations utilize the shock structures from Cropper et al. (1999) and the cyclotron opacity and radiative transfer from Meggitt & Wickramasinghe (1982) and Wickramasinghe & Meggitt (1985). The model is described by the WD mass, accretion rate, and magnetic field strength. The detailed morphology of the cyclotron emission, in particular the cyclotron humps, will depend

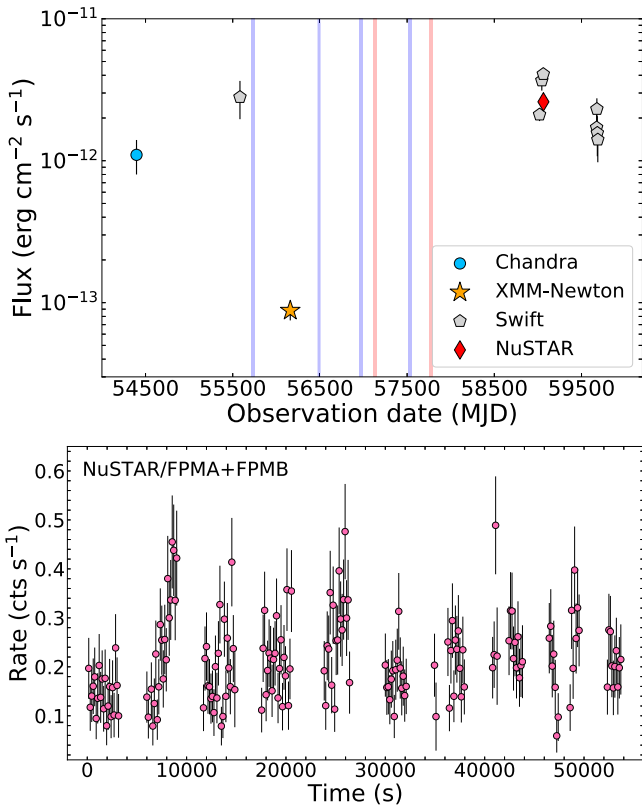


Figure 4. Top: long-term light curve (0.3–10 keV) of all X-ray observations included in this work. Vertical lines mark known times of high (blue) and low states (red) based on archival optical/IR observations. Bottom: background-subtracted NuSTAR light curve of J1654 in the 3–79 keV energy range. We combined the count rates from both FPMA and FPMB. The time bin is 150 s.

on the WD mass and accretion rate. However, the wavelength at which the cyclotron emission peaks is dominated by the magnetic field strength, with less influence from the WD mass and accretion rate. In the case of J1654, we are limited by the fact that we do not detect phase-dependent cyclotron humps in our optical spectroscopy, which would be required to obtain robust limits on the WD mass and accretion rate. Instead, we simply rescale the model (for a specific B field) to match the peak of the excess IR emission in Figure 5.

We find that if the IR excess is due to cyclotron radiation a low magnetic field strength of $B \lesssim 3.5$ MG is required. Any larger magnetic field would push the excess toward the optical. We have simply shown that if the main cause of the IR emission is cyclotron, then the magnetic field strength must be low to match the IR peak. We cannot, however, rule out the contribution of a circumbinary disk at these wavelengths (Brinkworth et al. 2007; Harrison & Campbell 2015). A circumbinary disk may reasonably explain the large extinction inferred from the SED. In either case, the lack of cyclotron humps in our phase-dependent optical spectra imply that a small magnetic field strength would be consistent with the excess from Spitzer. Despite the uncertainty in the spectral type of the secondary star, due to the similarity of the models (Figure 5), it does not change our estimate of the magnetic field.

We further note that the detection of the source in the *UVW1* filter by XMM-Newton/OM during the low state may indeed be the contribution of the WD. We consider this in both of the scenarios for the secondary star spectral type. In Figure 5, the dotted blue line shows the contribution of a thermal blackbody

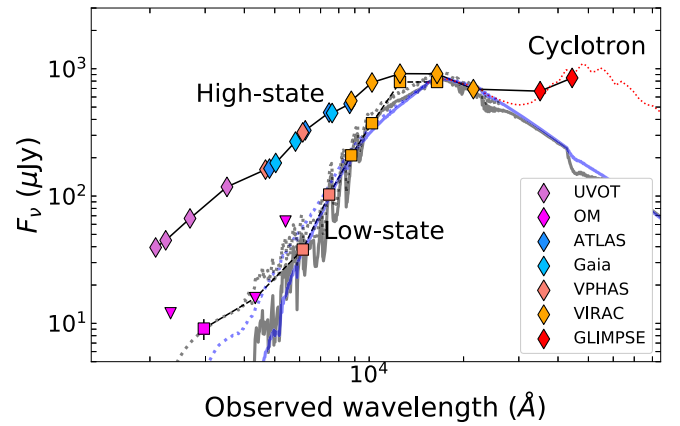


Figure 5. SED of the UV, optical, and IR counterpart to J1654. The solid black line connects photometry (diamonds) obtained during the high state, whereas the dashed black line (and squares) shows the low state. The data are not corrected for extinction; downward triangles represent 3σ upper limits. The thick, solid blue line shows the best-fit stellar model from ARIADNE (K dwarf), and the solid gray line is a less-extinct M dwarf (see Section 3.3). The dotted blue line represents the addition of a WD with $T = 120,000$ K and radius $R = 0.01 R_{\odot}$, modeled as a simple blackbody, with an extinction of $A_V \sim 4.9$ mag. The dotted gray line represents a WD with $T = 12,000$ K and extinction of $A_V \sim 0.5$ mag. The red dashed line is the addition of cyclotron emission from a polar with a magnetic field strength of 3.5 MG.

with $T = 120,000$ K at $d = 460$ pc added on top of the K dwarf model that has a large extinction ($A_V \sim 4.9$ mag). The high temperature is a direct result of the large extinction implied by the secondary star SED. In the M dwarf scenario, which implies a low extinction ($A_V \sim 0.5$ mag), we find a temperature of $T = 12,000$ K. These scenarios are quite different, and without further UV observations it is difficult to favor one over the other. An additional possibility is that the *UVW1* detection during the low state is still due to the accretion disk, and simply fainter due to a lower accretion rate.

3.4. Optical Spectroscopy

The initial optical spectrum of J1654 obtained with SALT (Section 2.1.3) is displayed in Figure 6. We detected a flat continuum with a slight blue slope, peppered with emission features. There are no obvious features related to the secondary star in the mean spectrum. In total, we identify 29 high-significance emission lines, including hydrogen lines of the Balmer and Paschen series, He I ($\lambda 3487$, $\lambda 3889$, $\lambda 4026$, $\lambda 4144$, $\lambda 4387$, $\lambda 4471$, $\lambda 4921$, $\lambda 5875$, $\lambda 6678$, $\lambda 7065$, and $\lambda 7281$), He II ($\lambda 4511$, $\lambda 4686$, and $\lambda 5411$), Ca II K, Mg I, O I, and the $\lambda 4640$ Bowen blend (a C III+N III line complex). The emission features are narrow (< 1000 km s $^{-1}$). This suggests emission from a hot spot, as opposed to the velocity-broadened inner regions of an accretion disk.

The wealth of helium lines, in particular He II $\lambda 4511$, $\lambda 4686$, and $\lambda 5411$, are characteristic of mCVs. We note that further He II lines (e.g., $\lambda 4101$, $\lambda 4340$, $\lambda 4861$, and $\lambda 6562$) are likely overlapping with the Balmer lines.

We use the observed line fluxes (Table 2) to compute the Balmer decrements. The line fluxes were determined by modeling each line as single Gaussian on top of the continuum emission. The ratios $H\alpha/H\beta \approx 1.36$ and $H\gamma/H\beta \approx 1.16$ have not been corrected for the uncertain Galactic extinction, but still signify an inverted Balmer decrement. The inverse Balmer decrement is in excess of expectations based on optically thin “case B” recombination (Pottasch 1984), and is, therefore,

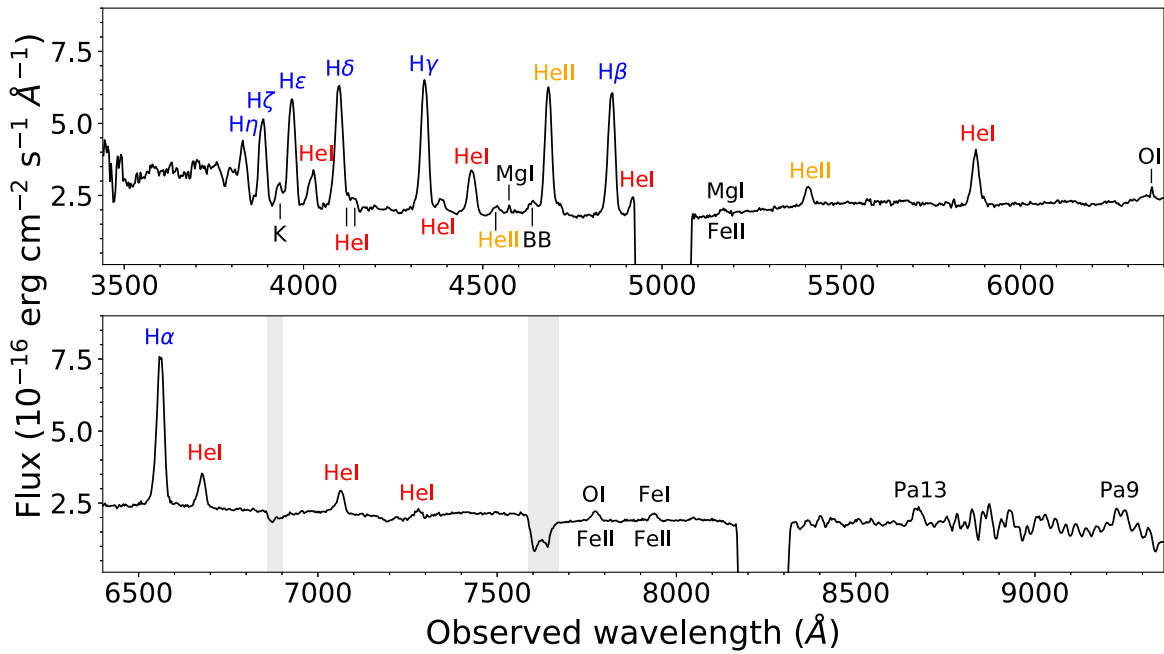


Figure 6. Mean spectrum of J1654 obtained with SALT. We have labeled the primary emission features: Balmer lines in blue, He I lines in red, He II lines in orange, and other features in black, including the Bowen blend (BB; N III/C III). Chips gaps are located at 5000 Å and 8250 Å. Gray vertical regions mark telluric features.

indicative of emission from an optically thick accretion region (Stockman et al. 1977; Williams 1980; Schwobe et al. 1997), typical of CVs. We further identify the observed ratio of $H\beta/H\alpha \approx 1.0$ as evidence that J1654 is a polar (Williams & Ferguson 1982; Williams 1989; Silber 1992).

If we assume $A_V \approx 4.9$ mag as derived in Section 3.3, we can correct the line fluxes using a Cardelli et al. (1989) Milky Way extinction law. This yields $H\alpha/H\beta \approx 0.3$, $H\gamma/H\beta \approx 2.5$, and $H\beta/He\ II\ \lambda 4686 \approx 0.76$. However, $A_V \approx 4.9$ mag is well above the $A_V \approx 0.13$ – 0.35 mag implied by Galactic dust maps over this distance range (Amôres & Lépine 2005; Amôres et al. 2021), which would yield ratios of order unity. We further note that the spectra do not appear significantly reddened nor are there significant Na I absorption lines, which would suggest a lower extinction than $A_V \approx 4.9$ mag. The order-unity line ratios, when not dereddened, further favor a lower extinction value.

Using the frame-transfer spectroscopy, we measured the radial velocities of $H\alpha$, $H\beta$, $H\gamma$, He II $\lambda 4686$, and He I $\lambda 5876$ by fitting Gaussian functions using the `lmfit` package (Newville et al. 2016) to derive the central wavelength, amplitude, and FWHM. The radial velocities of these lines as a function of phase are shown in Figure 7. The He I $\lambda 5876$ and He II $\lambda 4686$ lines display qualitatively similar behavior to the Balmer lines. This likely implies that the emission region is the same.

3.4.1. X-Ray Spectral Analysis

We performed a time-averaged spectral analysis of the Swift/XRT, XMM-Newton (MOS1/MOS2/PN), and NuSTAR (FPMA/FPMB) spectra using `XSPEC v12.12.0` (Arnaud 1996). We applied the interstellar medium abundance table from Wilms et al. (2000) and the photoelectric absorption cross sections presented by Verner et al. (1996). Spectral fits were performed in the 3–20 keV energy range for NuSTAR (the background dominates above 20 keV) and 0.3–10 keV for Swift and XMM-Newton. We determined the best-fit parameters by minimizing the Cash statistic (Cash 1979).

Table 2

Spectral Features Observed in the Mean SALT Spectrum from 2022 April 26

Feature	FWHM (Å)	Flux (erg cm ⁻² s ⁻¹)
H α	23.0	1.3×10^{-14}
H β	21.8	9.5×10^{-15}
H γ	22.8	1.1×10^{-14}
He II $\lambda 4686$	20.6	9.5×10^{-15}
He I $\lambda 5876$	22.5	4.3×10^{-15}

Note. The line fluxes have not been corrected for extinction.

We began by modeling the time-averaged PC mode spectrum for all XRT observations (10.3 ks). Individual shorter exposures yield large model uncertainties, and the time-averaged spectrum allows us to constrain the parameters better. The best-fit absorbed power-law model (`con*tbabs*pow`) has $N_H = (2.4 \pm 1.4) \times 10^{21}$ cm⁻² and $\Gamma = 1.46 \pm 0.25$. This yields a time-averaged unabsorbed flux $F_X = (2.56 \pm 0.30) \times 10^{-12}$ erg cm⁻² s⁻¹ in the 0.3–10 keV energy band. For these parameters, we derive an energy conversion factor (ECF) of 5.9×10^{-11} erg cm⁻² counts⁻¹, which we use to convert the count rates in individual exposures to an unabsorbed flux (Figure 4; top panel).

As all of the Swift observations occur within the high state, we performed a joint fit with the NuSTAR data, which were also obtained during the high state (Figure 4; top panel). Based on the source’s classification as an mCV (Takata et al. 2022), we tested three physically motivated models: (i) thermal bremsstrahlung radiation (`constant*tbabs*bremss`), likely caused as the magnetically funnelled accretion stream shocks above the WD poles; (ii) a cooling flow model (`constant*tbabs*mkcflow`) that self-consistently accounts for both bremsstrahlung radiation and line cooling (Mushotzky & Szymkowiak 1988); and, lastly, (iii) a model for bremsstrahlung radiation in the postshock structures (PSRs) of magnetized WDs

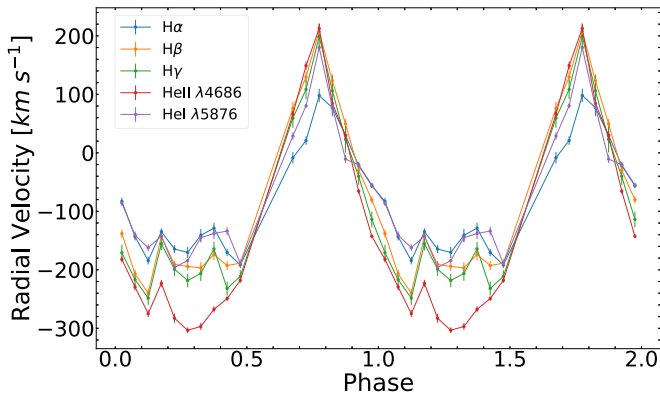


Figure 7. Radial velocity vs. orbital phase for the H α , H β , H γ , He II λ 4686, and He I λ 5876 emission lines.

(`constant*tbabs*ipolar`; Suleimanov et al. 2016, 2019). This last model is parameterized by the WD mass M_{WD} and relative magnetospheric radius R_m (hereafter referred to as the fall height). Following Shaw et al. (2020), we froze the fall height to $R_m = 1000 R_{\text{WD}}$. In the `mkcflow` model, we froze the redshift and `lowT` (hereafter T_{low}) parameters to their minimum values (10^{-7} and 0.0808 keV, respectively).

Each of these models provides a good description of the broadband spectrum (Cstat = 266–298 for 313 degrees of freedom (dof)). The results are recorded in Table 3, and we display the thermal bremsstrahlung radiation model in Figure 8. We note that the `mkcflow` and `ipolar` models yield consistent measurements for the WD mass. The measurement of the shock temperature $T_{\text{max}} = 21 \pm 3$ keV in the `mkcflow` is consistent with a WD mass of $M_{\text{WD}} = 0.59 \pm 0.06 M_{\odot}$ (Mukai 2017), which is the same as determined by `ipolar` ($M_{\text{WD}} = 0.58 \pm 0.05 M_{\odot}$). However, if cyclotron cooling is important (for high magnetic field strengths; $B > 20$ MG), then these models underestimate the WD mass. We therefore treat these measurements as a lower limit to the true WD mass. We do note, however, that our analysis in Section 3.3 suggests a low magnetic field strength.

We note that there is a hint of residuals in the 6–7 keV region of the Fe lines (see Figure 8), which can be reduced with the addition of a Gaussian emission line (`Gauss`) with fixed energy of 6.7 keV and fixed line width $\sigma = 0$ keV. Using the bremsstrahlung model, we set an equivalent width upper limit of < 210 eV. This constraint is within the range of reasonable values for other mCVs (Romanus et al. 2015).

We performed a similar analysis of the XMM-Newton data (PN/MOS1/MOS2) obtained in the low state. The data are sparse with almost no source photons at > 3 keV, and, therefore, we choose to only apply the power-law and bremsstrahlung models. We obtain a best fit for an absorbed power law (Cstat = 816 for 824 dof) with a low Galactic hydrogen column density $N_H = (8 \pm 5) \times 10^{20} \text{ cm}^{-2}$ and hard photon index $\Gamma = 1.6 \pm 0.2$. We derive an unabsorbed flux of $(8.8 \pm 1.3) \times 10^{-14} \text{ erg cm}^{-2} \text{ s}^{-1}$ in the 0.3–10 keV energy range, which is a factor of ~ 30 less than the flux observed with XRT. The low-state spectrum yields a smaller hydrogen column density, consistent with increased absorption during the high state, possibly due to the accretion column. We performed a test by applying the best-fit high-state model (only allowing the normalization to vary), and found that the increased absorption in the high state led to a model which underpredicted the low-state spectrum below 1 keV (consistent with a smaller absorption in the low state). We further note that there is no requirement for a soft X-ray excess, generally

described by a blackbody component with $T_{\text{bb}} < 100$ eV (Ramsay et al. 2001; Ramsay & Cropper 2004).

4. Discussion

Polars are often luminous soft X-ray sources. The number of known polars expanded greatly thanks to ROSAT (e.g., Burwitz et al. 1997, 1998; Reinsch et al. 1999). However, their systematic identification effort was limited to high Galactic latitudes for practical reasons (Thomas et al. 1998; Schwöpe et al. 2002), among which are the presence of many coronal (i.e., soft) sources dominating the 0.1–2.5 keV ROSAT band at low latitudes. First discovered by ROSAT, J1654 was identified through DGPS observations as an unclassified, relatively hard source coincident with a bright Gaia star. Based on these qualifiers, we observed the source with a variety of X-ray and optical instruments to aid in its classification. J1654 is yet another example of an X-ray-selected (0.3–10 keV) polar CV, initially discovered with ROSAT in soft X-rays, with a classification confirmed through optical spectroscopy and photometry (e.g., Thomas et al. 1998; Schwöpe et al. 2002; Beuermann et al. 2017, 2020, 2021). However, J1654 lies at low Galactic latitude, $b \approx 0.01^\circ$, demonstrating the importance of X-ray surveys, such as the Swift DGPS, with a broader energy coverage that can discriminate polars from coronal X-ray sources based on their hardness ratios.

The properties of J1654 outlined in the previous sections are characteristic of polars. The X-ray (0.3–10 keV) luminosity varies between $L_X = (6.5 \pm 0.8) \times 10^{31}$ and $(2.3 \pm 0.4) \times 10^{30} \text{ erg s}^{-1}$ in the high state and low state, respectively, assuming a distance of 460 pc. These luminosities suggest an accretion rate in the range of $(1\text{--}2) \times 10^{-11} M_{\odot} \text{ yr}^{-1}$. At these distances, the hard X-ray luminosity from Swift/BAT is $< 2 \times 10^{34} \text{ erg s}^{-1}$ in the 14–195 keV energy band. This is consistent with the range of hard X-ray luminosities of known polars (Suleimanov et al. 2022).

In the low state, the the hydrogen column density $N_{H,\text{low}} = (8 \pm 5) \times 10^{20} \text{ cm}^{-2}$ yields a Galactic extinction of $A_V = 0.36 \pm 0.23$ mag (Güver & Özel 2009). This is consistent with the low value of $A_V \approx 0.13\text{--}0.35$ mag (Amôres & Lépine 2005) derived from Galactic dust maps, but is at odds with the best-fitting SED (see Section 3.3). However, X-ray spectra obtained during the high state yield hydrogen column densities in the range $N_{H,\text{high}} = (2\text{--}5) \times 10^{21} \text{ cm}^{-2}$, which lead to a significantly larger $A_V \approx 1\text{--}2$ mag (Güver & Özel 2009). We therefore cannot rule out that there is significant extinction intrinsic to the source environment (e.g., a circumbinary disk). Further soft X-ray (0.3–10 keV) observations, preferably during the high state, with Swift, XMM-Newton, or eROSITA would be required to constrain the column density better.

Our analysis of the low-state SED implies a secondary star of late spectral type, consistent with the CV classification. We identify two main possibilities: (i) a K dwarf with large extinction $A_V \sim 4.9$ mag and (ii) an M dwarf with smaller extinction $A_V \sim 0.5$ mag. On balance we prefer the latter scenario for multiple reasons. First, the M dwarf scenario has better agreement with the inferred extinction values using the low-state X-ray spectra ($N_{H,\text{low}}$), as well as Galactic dust maps. Second, a smaller value of the extinction has better agreement with Balmer decrements of order unity in our optical spectra, matching predictions for CVs. Third, interpreting the *UVW1* detection in the low state as emission from a WD leads to an estimate of the WD temperature of $T = 12,000$ K, which is consistent with typical temperatures of accreting WDs (Szkody et al. 2010; Pala et al. 2017).

Table 3
Results of Our X-Ray Spectral Fitting

Parameter	Units	Model			
		pow	bremss	mkcflow	ipolar
High State					
N_H	10^{22} cm^{-2}	0.49 ± 0.07	0.24 ± 0.05	0.35 ± 0.05	0.28 ± 0.05
Γ	...	2.02 ± 0.07
N_{pow}	$10^{-4} \text{ ph cm}^{-2} \text{ s}^{-1}$	8.1 ± 1.3
kT	keV	...	10.1 ± 1.2
N_{bremss}	10^{-4}	...	5.4 ± 0.4
T_{high}	keV	21 ± 3	...
A^a	0.8 ± 0.3	...
N_{mkcflow}	$10^{-12} M_{\odot} \text{ yr}^{-1}$	20 ± 4	...
M_{WD}	M_{\odot}	0.58 ± 0.06
R_m/R_{WD}	1000
N_{ipolar}	10^{-28}	5.0 ± 1.7
C_{FPMA}	...	1.0	1.0	1.0	1.0
C_{FPMB}	...	0.94 ± 0.07	0.94 ± 0.07	0.94 ± 0.07	0.94 ± 0.07
C_{XRT}	...	0.63 ± 0.07	0.76 ± 0.07	0.72 ± 0.08	0.75 ± 0.08
C_{stat}	...	298/313	268/313	266/312	273/313
Low State					
N_H	10^{22} cm^{-2}	$(8 \pm 5) \times 10^{-2}$	$(5 \pm 3) \times 10^{-2}$
Γ	...	1.6 ± 0.2
N_{pow}	$10^{-4} \text{ ph cm}^{-2} \text{ s}^{-1}$	0.12 ± 0.02
kT	keV	...	8_{-3}^{+9}
N_{bremss}	10^{-4}	...	0.15 ± 0.02
C_{PN}	...	1.0	1.0
C_{MOS1}	...	0.84 ± 0.18	0.82 ± 0.16
C_{MOS2}	...	1.05 ± 0.20	1.04 ± 0.19
$C_{\text{stat/dof}}$...	816/824	816/824

Note. The high-state data include our Swift and NuSTAR (FPMA and FPMB) spectra, while the low-state data include only the archival XMM-Newton (PN, MOS1, and MOS2) data.

^a Abundance relative to solar in the `mkcflow` model.

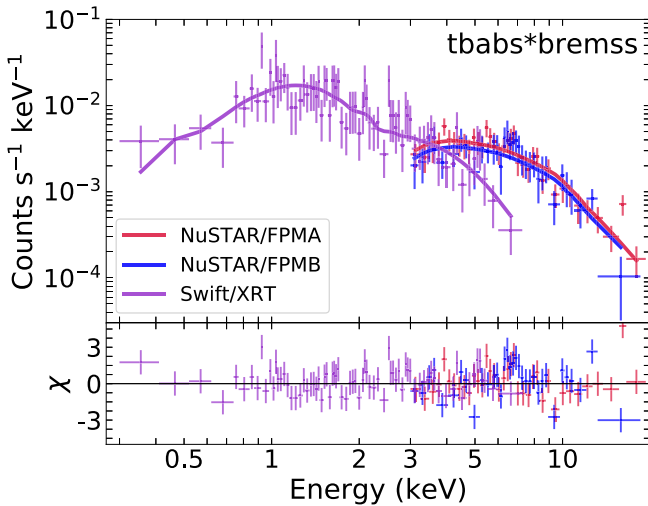


Figure 8. X-ray spectra of J1654 in the high state from Swift and NuSTAR. The best-fit model (`con*tbabs*bremss`) is shown. The spectra have been rebinned for display purposes. There is a hint of an Fe $K\alpha$ line at 6.7 keV in the NuSTAR spectra.

Our classification of the source as a polar agrees with the interpretation of Takata et al. (2022), who classified the source as a candidate polar, though they did not exclude an IP classification. In this work, we further exclude the possibility that the source is an IP and solidify the polar classification for the following reasons. First,

both our analysis and that of Takata et al. (2022) identify only a single period of 2.87 hr. In the polar interpretation, this period is $P_{\text{orb}} = P_{\text{spin}}$. However, if the system is interpreted as an IP then the spin period must be less than the orbital period, and the 2.87 hr period must be one or the other. While 2.87 hr can be the orbital period of an IP, the phase-folded TESS light curve presented by Takata et al. (2022; their Figure 17) shows a primary maximum lasting half a cycle, with a sharp rise and sharp decline. This is atypical compared to other IPs. Given that much of the optical light from an IP is from the partial accretion disk, which is more or less axially symmetric, there is no ready explanation for such an orbital modulation. In fact, optical photometric variability of the orbital period is usually of low amplitude in IPs, and is more gradual in waveform, unless there is an eclipse, to the point that the large majority of orbital period determinations are determined from optical spectroscopy (for examples of the period determinations in IPs see, e.g., Falomo et al. 1987; Hellier & Sproats 1992; Haberl et al. 1994; Remillard et al. 1994; Allan et al. 1999; Norton et al. 2002; Zharikov et al. 2002; de Martino et al. 2006; Scaringi et al. 2011; Aungwerojwit et al. 2012; Halpern et al. 2018; Gorgone et al. 2021).

We must also consider the possibility that the 2.87 hr period is the spin period of the WD. This conflicts with known IP systems, where all but three of the 71 confirmed IPs³⁶ have spin periods shorter than 1 hr. Therefore, this interpretation would

³⁶ <https://asd.gsfc.nasa.gov/Koji.Mukai/iphome/catalog/alpha.html>

make J1654 the longest spin period IP, significantly longer than the previous record holder (RX J2015.6+3711 at 7196 s, or just under 2 hr; Halpern & Thorstensen 2015; Coti Zelati et al. 2016). Note that RX J2015.6+3711 has an orbital period of 12.76 hr and that the spectral features of the secondary are readily detectable in optical spectra during its normal (high accretion rate) state (Halpern et al. 2018). In general, if J1654 is an IP with a 2.87 hr spin period, this would likely require an orbital period significantly longer than a few hours. In contrast, the low-state SED indicates a small mass donor consistent with the size of the Roche lobe for a ~ 3 hr orbital period CV (Knigge et al. 2011). Therefore, we conclude that the interpretation of J1654 as a polar is the most probable explanation, and that it matches all available information for the source.

With an orbital period of 2.87 hr, J1654 lies within the CV period gap. This is a common property of polars, which do not exhibit a prominent period gap (Wickramasinghe & Wu 1994; Webbink & Wickramasinghe 2002). This is thought to be due to reduced magnetic braking affecting the evolution of polars, see, e.g., Li et al. (1994) and Belloni et al. (2020). We discuss the validity of this interpretation for J1654 in more detail below.

We are confident that, if the IR excess from Spitzer is due to cyclotron radiation, the magnetic field has to be rather low ($B \approx 3.5$ MG). This is also supported by the fact that larger magnetic field strengths begin to push the excess toward the optical, where we would expect to observe cyclotron bumps in our SALT spectra (e.g., Figure 6).

Furthermore, based on the X-ray luminosity we infer an accretion rate of $\sim 10^{-11} M_{\odot} \text{ yr}^{-1}$. While some adjustment is needed to account for the accretion power that goes into cyclotron emission, the correction is likely small due to the fact that we do not detect a luminous soft X-ray component (Ramsay & Cropper 2004). On the other hand, the inferred rate is based on a single measurement during a high state, and the long-term average (over high and low states) is likely somewhat, but not greatly, lower. This is because Figure 4 suggests that this polar is usually found in a high state (four out of five epochs since 2007; grouping the XRT observations of a similar time into the same epoch). This should be compared to the 21 out of 37 polars found in a high state by Ramsay et al. (2004).

In any case, the accretion rate is comparable to the expected values for systems whose evolution is driven purely by gravitational wave radiation (e.g., Knigge et al. 2011). This is consistent with the reduced magnetic braking model for the evolution of polars (Li et al. 1994; Belloni et al. 2020), in which the magnetic braking mechanism is ineffective for polars due to the WD's magnetic field. However, there is tension between this conclusion and the low magnetic field ($B \approx 3.5$ MG) that was obtained by modeling the IR excess as cyclotron emission: can such a low field nevertheless reduce magnetic braking, and if so, should we not see a similar effect in IPs?

Further optical and IR observations, including IR spectroscopy, and a more secure determination of the magnetic field, is highly desirable. In particular, optical and IR spectroscopy to identify the phase-dependent cyclotron humps are required before a detailed modeling of the WD mass, accretion rate, and magnetic field can be performed. IR spectroscopy may either confirm or exclude cyclotron emission as the nature of the IR excess, and is therefore strongly encouraged.

5. Conclusions

We have presented the results of the DGPS multiwavelength follow-up campaign of J1654 using Swift, NuSTAR, SAAO, and SALT. The source displays a hard X-ray spectrum in the high state characterized by thermal bremsstrahlung radiation with temperature $kT = 10.1 \pm 1.2$ keV and luminosity $\sim 6.5 \times 10^{31} \text{ erg s}^{-1}$. The low-state luminosity, revealed by archival XMM-Newton data, is a factor of ~ 30 fainter.

Moreover, we identify the UV, optical, and IR counterpart using archival Chandra observations. A SALT spectrum of the source revealed a variety of emission lines of hydrogen and helium, and demonstrated an inverse Balmer decrement. High-speed photometry with the 1 m SAAO over multiple nights in 2022 May and June allowed us to derive an orbital period of 2.87 hr. The X-ray, UV, optical, IR, and, in particular, emission line, properties allow us to classify J1654 as a polar. This classification is in agreement with the independent analysis of Takata et al. (2022).

Acknowledgments

The authors thank the anonymous referee for their careful review and constructive feedback. B.O. would like to acknowledge the significant contribution of Nicholas Gorgone to DGPS operations and analyses during his dissertation research. B.O. acknowledges useful discussions with Jeremy Hare. B.O. and C.K. acknowledge support from NASA grant 80NSSC20K0389.

This work is based on observations obtained with the Southern African Large Telescope under program 2021-2-LSP-001. This work made use of data supplied by the UK Swift Science Data Centre at the University of Leicester. This research has made use of the XRT Data Analysis Software (XRTDAS) developed under the responsibility of the ASI Science Data Center (ASDC), Italy. This work made use of data from the NuSTAR mission, a project led by the California Institute of Technology, managed by the Jet Propulsion Laboratory, and funded by the National Aeronautics and Space Administration. This research has made use of the NuSTAR Data Analysis Software (NuSTARDAS) jointly developed by the ASI Space Science Data Center (SSDC, Italy) and the California Institute of Technology (Caltech, USA). This research has made use of data and/or software provided by the High Energy Astrophysics Science Archive Research Center (HEASARC), which is a service of the Astrophysics Science Division at NASA/GSFC. The scientific results reported in this article are based on observations made by the Chandra X-ray Observatory. This research has made use of data obtained from the 4XMM XMM-Newton serendipitous stacked source catalog 4XMM-DR11s compiled by the institutes of the XMM-Newton Survey Science Centre selected by ESA.

Facilities: Swift, NuSTAR, XMM, SALT, Elizabeth

Software: HEASoft 6.29c, XRTDAS, NuSTARDAS, SAS, XSPEC (Arnaud 1996), IRAF (Tody 1986), Astropy (Astropy Collaboration et al. 2013), ARIADNE (Vines & Jenkins 2022), and *dynesty* (Speagle 2020).

Appendix A Log of Observations

Here we present tables reporting the log of X-ray (Table A1), UV (Table A2), and optical (SALT; Table A3) observations in this work.

Table A1
Log of X-Ray Observations Used in This Work

Start Time (UT)	Telescope	Instrument	Exposure (s)	ObsID
2007-10-23 15:22:50	Chandra	HRC-I	1590	8231
2011-01-21 23:47:59	Swift	XRT	496	00043184001
2012-08-20 21:58:28	XMM-Newton	MOS1/MOS2/PN	14,916	0695000301
2020-06-18 06:40:36	Swift	XRT	3941	03110780002 ^a
2020-07-14 12:10:35	Swift	XRT	1003	03110780003 ^a
2020-07-31 13:30:36	Swift	XRT	1727	00089169001 ^a
2020-08-02 03:54:59	NuSTAR	FPMA/B	25,655	90601324002 ^b
2022-04-04 03:17:00	Swift	XRT	855	00043184003 ^b
2022-04-07 02:58:00	Swift	XRT	950	00043184004 ^b
2022-04-12 11:56:00	Swift	XRT	990	00043184005 ^b
2022-04-17 16:04:00	Swift	XRT	760	00043184006 ^b

Notes.^a DGPS observation.^b DGPS ToO.

Table A2
Log of UV Observations of J1654

Start Time (UT)	Telescope	Instrument	ObsID	Filter	Exposure (s)	AB mag
2011-01-21 23:49:44	Swift	UVOT	00043184001	<i>uvm2</i>	494	19.77 ± 0.11
2012-08-20 22:07:32	XMM-Newton	OM	0695000301	<i>V</i>	1500	>19.4
2012-08-20 22:37:39	XMM-Newton	OM	0695000301	<i>B</i>	1900	>20.9
2012-08-20 23:14:26	XMM-Newton	OM	0695000301	<i>UVW1</i>	5000	21.5 ± 0.2
2012-08-21 00:42:53	XMM-Newton	OM	0695000301	<i>UVW2</i>	5000	>21.2
2020-06-18 06:46:54	Swift	UVOT	03110780002	<i>uvw1</i>	301	19.27 ± 0.12
2020-06-18 13:16:15	Swift	UVOT	03110780002	<i>uvw1</i>	820	19.24 ± 0.07
2020-06-18 14:27:56	Swift	UVOT	03110780002	<i>uvw1</i>	899	19.34 ± 0.07
2020-06-18 17:59:39	Swift	UVOT	03110780002	<i>uvw1</i>	676	19.45 ± 0.08
2020-06-18 21:01:41	Swift	UVOT	03110780002	<i>uvw1</i>	674	19.22 ± 0.07
2020-06-18 22:49:21	Swift	UVOT	03110780002	<i>uvw1</i>	521	19.42 ± 0.09
2020-07-14 12:15:02	Swift	UVOT	03110780003	<i>uvw1</i>	475	19.33 ± 0.10
2020-07-14 18:37:13	Swift	UVOT	03110780003	<i>uvw1</i>	524	19.36 ± 0.10
2020-07-31 13:35:09	Swift	UVOT	00089169001	<i>uvw2</i>	1726	19.91 ± 0.07
2022-04-04 03:19:46	Swift	UVOT	00043184003	<i>uvw2</i>	850	19.67 ± 0.08
2022-04-07 02:59:10	Swift	UVOT	00043184004	<i>u</i>	946	18.72 ± 0.10
2022-04-12 11:59:50	Swift	UVOT	00043184005	<i>uvw2</i>	186	20.21 ± 0.24
2022-04-12 13:37:41	Swift	UVOT	00043184005	<i>uvw2</i>	434	19.80 ± 0.12
2022-04-12 15:16:01	Swift	UVOT	00043184005	<i>uvw2</i>	354	19.94 ± 0.15
2022-04-17 16:05:13	Swift	UVOT	00043184006	<i>uvm2</i>	523	19.84 ± 0.12
2022-04-17 22:38:07	Swift	UVOT	00043184006	<i>uvm2</i>	229	19.90 ± 0.19

Table A3
Log of SALT and SAAO Observations of J1654

Start Time (UT)	Telescope	Mode	Grating	Filter	Duration (hr)
Optical Spectroscopy					
2022-04-26 22:12:39	SALT	LS	PG0300	...	0.42
2022-05-02 21:24:20	SALT	FT	PG0900	...	0.83
2022-05-10 03:05:48	SALT	FT	PG0900	...	0.83
2022-05-27 02:10:09	SALT	FT	PG0900	...	0.70
High-speed Optical Photometry					
2022-05-04 21:33:00	SAAO	HSP—5 s	...	<i>clear</i>	6.9
2022-05-05 21:07:00	SAAO	HSP—5 s	...	<i>clear</i>	6.3
2022-05-08 20:54:00	SAAO	HSP—5 s	...	<i>i'</i>	6.9
2022-05-09 20:45:00	SAAO	HSP—10 s	...	<i>g'</i>	7.1
2022-06-01 19:42:00	SAAO	HSP—10 s	...	<i>i'</i>	8.4
2022-06-02 19:39:00	SAAO	HSP—5 s	...	<i>r'</i>	8.3
2022-06-07 22:18:00	SAAO	HSP—10 s	...	<i>g'</i>	4.1
2022-06-08 20:07:00	SAAO	HSP—10 s	...	<i>i'</i>	3.1

Note. The modes refer to longslit (LS) spectroscopy, frame-transfer (FT) spectroscopy, or high-speed photometry (HSP) with an exposure time of either 5 or 10 s.

Appendix B Secondary Star Modeling

Here we show the corner plot (Figure B1) derived using ARIADNE (Vines & Jenkins 2022). The best-fit model is displayed in Figure 5.

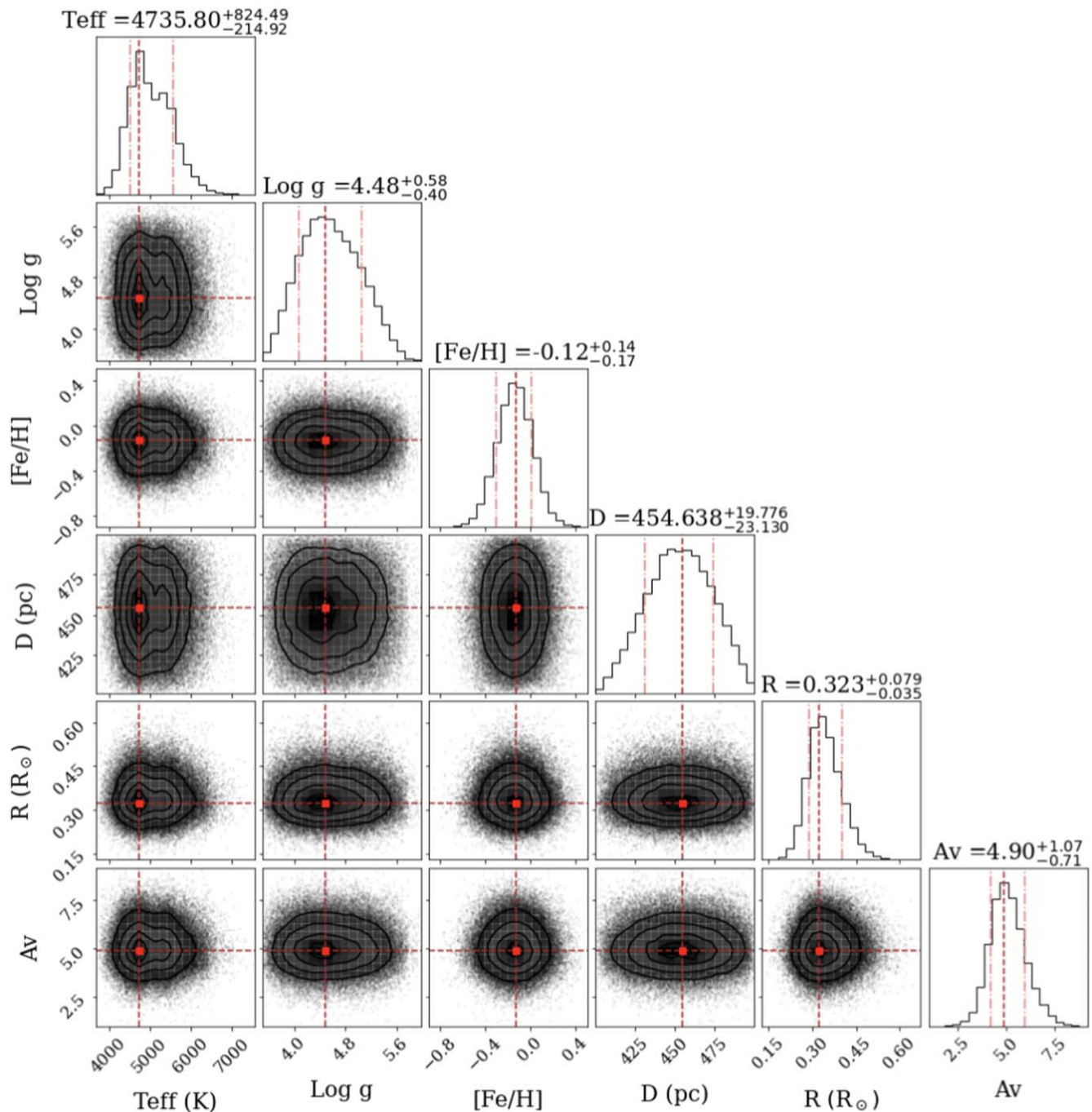


Figure B1. Corner plot of secondary star parameters derived from modeling the low-state SED with ARIADNE.

ORCID iDs

B. O'Connor <https://orcid.org/0000-0002-9700-0036>
 J. Brink <https://orcid.org/0000-0003-0030-7566>
 D. A. H. Buckley <https://orcid.org/0000-0002-7004-9956>
 K. Mukai <https://orcid.org/0000-0002-8286-8094>
 C. Kouveliotou <https://orcid.org/0000-0003-1443-593X>
 E. Göğüş <https://orcid.org/0000-0002-5274-6790>
 S. B. Potter <https://orcid.org/0000-0002-5956-2249>
 P. Woudt <https://orcid.org/0000-0002-6896-1655>
 A. Lien <https://orcid.org/0000-0002-7851-9756>
 A. Levan <https://orcid.org/0000-0001-7821-9369>
 O. Kargaltsev <https://orcid.org/0000-0002-6447-4251>
 M. G. Baring <https://orcid.org/0000-0003-4433-1365>

E. Bellm <https://orcid.org/0000-0001-8018-5348>
 S. B. Cenko <https://orcid.org/0000-0003-1673-970X>
 P. A. Evans <https://orcid.org/0000-0002-8465-3353>
 J. Granot <https://orcid.org/0000-0001-8530-8941>
 C. Hailey <https://orcid.org/0000-0002-3681-145X>
 F. Harrison <https://orcid.org/0000-0002-4226-8959>
 D. Hartmann <https://orcid.org/0000-0002-8028-0991>
 A. J. van der Horst <https://orcid.org/0000-0001-9149-6707>
 D. Huppenkothen <https://orcid.org/0000-0002-1169-7486>
 J. A. Kennea <https://orcid.org/0000-0002-6745-4790>
 P. O. Slane <https://orcid.org/0000-0002-6986-6756>
 D. Stern <https://orcid.org/0000-0003-2686-9241>
 E. Troja <https://orcid.org/0000-0002-1869-7817>

R. A. M. J. Wijers  <https://orcid.org/0000-0002-3101-1808>
 G. Younes  <https://orcid.org/0000-0002-7991-028X>

References

- Allan, A., Hellier, C., & Buckley, D. A. H. 1999, in ASP Conf. Ser. 157, Annapolis Workshop on Magnetic Cataclysmic Variables, ed. C. Hellier & K. Mukai (San Francisco, CA: ASP), 57
- Amôres, E. B., Jesus, R. M., Moitinho, A., et al. 2021, *MNRAS*, 508, 1788
- Amôres, E. B., & Lépine, J. R. D. 2005, *AJ*, 130, 659
- Anderson, G. E., Gaensler, B. M., Kaplan, D. L., et al. 2014, *ApJS*, 212, 13
- Arnaud, K. A. 1996, in ASP Conf. Ser. 101, Astronomical Data Analysis Software and Systems V, ed. G. H. Jacoby & J. Barnes (San Francisco, CA: ASP), 17
- Astropy Collaboration, Robitaille, T. P., Tollerud, E. J., et al. 2013, *A&A*, 558, A33
- Aungwerojwit, A., Gänsicke, B. T., Wheatley, P. J., et al. 2012, *ApJ*, 758, 79
- Bailer-Jones, C. A. L., Rybizki, J., Fousneau, M., Demleitner, M., & Andrae, R. 2021, *AJ*, 161, 147
- Bailer-Jones, C. A. L., Rybizki, J., Fousneau, M., Mantelet, G., & Andrae, R. 2018, *AJ*, 156, 58
- Bailey, J. 1981, *MNRAS*, 197, 31
- Barthelmy, S. D., Barbier, L. M., Cummings, J. R., et al. 2005, *SSRv*, 120, 143
- Baumgartner, W. H., Tueller, J., Markwardt, C. B., et al. 2013, *ApJS*, 207, 19
- Belloni, D., Schreiber, M. R., Pala, A. F., et al. 2020, *MNRAS*, 491, 5717
- Benjamin, R. A., Churchwell, E., Babler, B. L., et al. 2003, *PASP*, 115, 953
- Bernardini, F., de Martino, D., Falanga, M., et al. 2012, *A&A*, 542, A22
- Beuermann, K., Burwitz, V., Reinsch, K., Schwöpe, A., & Thomas, H. C. 2017, *A&A*, 603, A47
- Beuermann, K., Burwitz, V., Reinsch, K., Schwöpe, A., & Thomas, H. C. 2020, *A&A*, 634, A91
- Beuermann, K., Burwitz, V., Reinsch, K., Schwöpe, A., & Thomas, H. C. 2021, *A&A*, 645, A56
- Bowman, D. M., & Holdsworth, D. L. 2019, *A&A*, 629, A21
- Breeveld, A. A., Landsman, W., Holland, S. T., et al. 2011, in AIP Conf. Ser. 1358, Gamma Ray Bursts 2010, ed. J. E. McEnery, J. L. Racusin, & N. Gehrels (Melville, NY: AIP), 373
- Brinkworth, C. S., Hoard, D. W., Wachter, S., et al. 2007, *ApJ*, 659, 1541
- Buccheri, R., Bennett, K., Bignami, G. F., et al. 1983, *A&A*, 128, 245
- Buckley, D. A. H., Swart, G. P., & Meiring, J. G. 2006, *Proc. SPIE*, 6267, 62670Z
- Burgh, E. B., Nordsieck, K. H., Kobulnicky, H. A., et al. 2003, *Proc. SPIE*, 4841, 1463
- Burrows, D. N., Hill, J. E., Nousek, J. A., et al. 2005, *SSRv*, 120, 165
- Burwitz, V., Reinsch, K., Beuermann, K., & Thomas, H. C. 1997, *A&A*, 327, 183
- Burwitz, V., Reinsch, K., Schwöpe, A. D., et al. 1998, *A&A*, 331, 262
- Cardelli, J. A., Clayton, G. C., & Mathis, J. S. 1989, *ApJ*, 345, 245
- Cash, W. 1979, *ApJ*, 228, 939
- Castelli, F., & Kurucz, R. L. 2003, in IAU Symp. 210, Modelling of Stellar Atmospheres, ed. N. Piskunov, W. W. Weiss, & D. F. Gray (Cambridge: Cambridge Univ. Press), A20
- Coppejans, R., Gulbis, A. A. S., Kotze, M. M., et al. 2013, *PASP*, 125, 976
- Coti Zelati, F., Rea, N., Campana, S., et al. 2016, *MNRAS*, 456, 1913
- Crawford, S. M., Still, M., Schellart, P., et al. 2010, *Proc. SPIE*, 7737, 77372S
- Cropper, M. 1990, *SSRv*, 54, 195
- Cropper, M., Wu, K., Ramsay, G., & Kocabiyyik, A. 1999, *MNRAS*, 306, 684
- de Martino, D., Bonnet-Bidaud, J. M., Mouchet, M., et al. 2006, *A&A*, 449, 1151
- Drew, J. E., Gonzalez-Solares, E., Greimel, R., et al. 2014, *MNRAS*, 440, 2036
- Evans, I. N., Primi, F. A., Glotfelty, K. J., et al. 2010, *ApJS*, 189, 37
- Evans, P. A., Beardmore, A. P., Page, K. L., et al. 2009, *MNRAS*, 397, 1177
- Falomo, R., Bonnet-Bidaud, J. M., Charles, P. A., et al. 1987, *Ap&SS*, 131, 631
- Gaia Collaboration 2020, *yCat*, I/350
- Gaia Collaboration, Brown, A. G. A., Vallenari, A., et al. 2016, *A&A*, 595, A2
- Gaia Collaboration, Brown, A. G. A., Vallenari, A., et al. 2018, *A&A*, 616, A1
- Gorgone, N. M., Woudt, P. A., Buckley, D., et al. 2021, arXiv:2103.14800
- Güver, T., & Özel, F. 2009, *MNRAS*, 400, 2050
- Haberl, F., Thorstensen, J. R., Motch, C., et al. 1994, *A&A*, 291, 171
- Halpern, J. P., & Thorstensen, J. R. 2015, *AJ*, 150, 170
- Halpern, J. P., Thorstensen, J. R., Cho, P., et al. 2018, *AJ*, 155, 247
- Harrison, T. E., & Campbell, R. K. 2015, *ApJS*, 219, 32
- Hellier, C., & Sproats, L. N. 1992, *IBVS*, 3724, 1
- Hessman, F. V., Gänsicke, B. T., & Mattei, J. A. 2000, *A&A*, 361, 952
- Husser, T.-O., von Berg, S. W., Dreizler, S., et al. 2013, *A&A*, 553, A6
- Knigge, C. 2006, *MNRAS*, 373, 484
- Knigge, C., Baraffe, I., & Patterson, J. 2011, *ApJS*, 194, 28
- Kobulnicky, H. A., Nordsieck, K. H., Burgh, E. B., et al. 2003, *Proc. SPIE*, 4841, 1634
- Krimm, H. A., Holland, S. T., Corbet, R. H. D., et al. 2013, *ApJS*, 209, 14
- Kurucz, R. L. 1979, *ApJS*, 40, 1
- Li, J. K., Wu, K. W., & Wickramasinghe, D. T. 1994, *MNRAS*, 268, 61
- Lien, A., Sakamoto, T., Barthelmy, S. D., et al. 2016, *ApJ*, 829, 7
- Mason, K. O., Breeveld, A., Much, R., et al. 2001, *A&A*, 365, L36
- Meggitt, S. M. A., & Wickramasinghe, D. T. 1982, *MNRAS*, 198, 71
- Minniti, D., Lucas, P., & VVV Team 2017, *yCat*, II/348
- Mukai, K. 2017, *PASP*, 129, 062001
- Mushotzky, R. F., & Szymkowiak, A. E. 1988, in Cooling Flows in Clusters and Galaxies, ed. A. C. Fabian (Dordrecht: Springer), 53
- Newville, M., Stensitzki, T., Allen, D. B., et al., 2016 Lmfit: Non-Linear Least-Square Minimization and Curve-Fitting for Python, Astrophysics Source Code Library, ascl:1606.014
- Norton, A. J., Quaintrell, H., Katajainen, S., et al. 2002, *A&A*, 384, 195
- O'Connor, B., Kouveliotou, C., Evans, P. A., et al. 2023a, arXiv:2306.14354
- O'Connor, B., Göğüş, E., Hare, J., et al. 2023b, *MNRAS*, 525, 5015
- Oh, K., Koss, M., Markwardt, C. B., et al. 2018, *ApJS*, 235, 4
- Oliveira, A. S., Rodrigues, C. V., Cieslinski, D., et al. 2017, *AJ*, 153, 144
- Oliveira, A. S., Rodrigues, C. V., Martins, M., et al. 2020, *AJ*, 159, 114
- Pala, A. F., Gänsicke, B. T., Breedt, E., et al. 2020, *MNRAS*, 494, 3799
- Pala, A. F., Gänsicke, B. T., Townsley, D., et al. 2017, *MNRAS*, 466, 2855
- Parsons, S. G., Gänsicke, B. T., Marsh, T. R., et al. 2018, *MNRAS*, 481, 1083
- Patterson, J. 1994, *PASP*, 106, 209
- Pottasch, S. R. 1984, Planetary Nebulae. A Study of Late Stages of Stellar Evolution (Dordrecht: Reidel)
- Potter, S., Ramsay, G., Wu, K., & Cropper, M. 2002, in ASP Conf. Ser. 261, The Physics of Cataclysmic Variables and Related Objects, ed. B. T. Gänsicke, K. Beuermann, & K. Reinsch (San Francisco, CA: ASP), 165
- Ramsay, G., & Cropper, M. 2004, *MNRAS*, 347, 497
- Ramsay, G., Cropper, M., Córdova, F., et al. 2001, *MNRAS*, 326, L27
- Ramsay, G., Cropper, M., Wu, K., et al. 2004, *MNRAS*, 350, 1373
- Reinsch, K., Burwitz, V., Beuermann, K., & Thomas, H.-C. 1999, in ASP Conf. Ser. 157, Annapolis Workshop on Magnetic Cataclysmic Variables, ed. C. Hellier & K. Mukai (San Francisco, CA: ASP), 187
- Remillard, R. A., Bradt, H. V., Brissenden, R. J. V., et al. 1994, *ApJ*, 428, 785
- Reynolds, M. T., Miller, J. M., Maitra, D., et al. 2013, *ATel*, 5200, 1
- Romanou, E., Saitou, K., & Ebisawa, K. 2015, arXiv:1511.09424
- Roming, P. W. A., Kennedy, T. E., Mason, K. O., et al. 2005, *SSRv*, 120, 95
- Sakamoto, T., Barthelmy, S. D., Baumgartner, W. H., et al. 2011, *ApJS*, 195, 2
- Scargle, J. D. 1982, *ApJ*, 263, 835
- Scaringi, S., Connolly, S., Patterson, J., et al. 2011, *A&A*, 530, A6
- Schwöpe, A. D., Brunner, H., Buckley, D., et al. 2002, *A&A*, 396, 895
- Schwöpe, A. D., Buckley, D. A. H., O'Donoghue, D., et al. 1997, *A&A*, 326, 195
- Shaw, A. W., Heinke, C. O., Mukai, K., et al. 2020, *MNRAS*, 498, 3457
- Silber, A. D. 1992, PhD thesis, Massachusetts Institute of Technology
- Smith, L. C., Lucas, P. W., Kurtev, R., et al. 2018, *MNRAS*, 474, 1826
- Smith, M. P., Nordsieck, K. H., Burgh, E. B., et al. 2006, *Proc. SPIE*, 6269, 62692A
- Speagle, J. S. 2020, *MNRAS*, 493, 3132
- Stockman, H. S., Schmidt, G. D., Angel, J. R. P., et al. 1977, *ApJ*, 217, 815
- Suleimanov, V., Doroshenko, V., Ducci, L., Zhukov, G. V., & Werner, K. 2016, *A&A*, 591, A35
- Suleimanov, V. F., Doroshenko, V., & Werner, K. 2019, *MNRAS*, 482, 3622
- Suleimanov, V. F., Doroshenko, V., & Werner, K. 2022, *MNRAS*, 511, 4937
- Szkody, P., Diczko, B., Ho, A. Y. Q., et al. 2020, *AJ*, 159, 198
- Szkody, P., Mukadam, A., Gänsicke, B. T., et al. 2010, *ApJ*, 710, 64
- Takata, J., Wang, X. F., Kong, A. K. H., et al. 2022, *ApJ*, 936, 134
- Thomas, H. C., Beuermann, K., Reinsch, K., et al. 1998, *A&A*, 335, 467
- Tody, D. 1986, *Proc. SPIE*, 627, 733
- Tonry, J. L., Denneau, L., Flewelling, H., et al. 2018, *ApJ*, 867, 16
- Traulsen, I., Schwöpe, A. D., Lamer, G., et al. 2020, *A&A*, 641, A137
- Vanderplas, J. 2015, Gatspy: General Tools For Astronomical Time Series In Python, v0.1.1, Zenodo, doi:10.5281/zenodo.14833
- Verner, D. A., Ferland, G. J., Korista, K. T., & Yakovlev, D. G. 1996, *ApJ*, 465, 487
- Vines, J. I., & Jenkins, J. S. 2022, *MNRAS*, 513, 2719
- Warner, B. 1987, *MNRAS*, 227, 23
- Warner, B. 1995, Cataclysmic Variable Stars (Cambridge: Cambridge Univ. Press), 592

Warner, B. 1999, in ASP Conf. Ser. 157, Annapolis Workshop on Magnetic Cataclysmic Variables, ed. C. Hellier & K. Mukai (San Francisco, CA: ASP), 63
Webbink, R. F., & Wickramasinghe, D. T. 2002, [MNRAS](#), 335, 1
Wickramasinghe, D. T., & Meggitt, S. M. A. 1985, [MNRAS](#), 214, 605
Wickramasinghe, D. T., & Wu, K. 1994, [MNRAS](#), 266, L1

Williams, R. E. 1980, [ApJ](#), 235, 939
Williams, R. E. 1989, [AJ](#), 97, 1752
Williams, R. E., & Ferguson, D. H. 1982, [ApJ](#), 257, 672
Wilms, J., Allen, A., & McCray, R. 2000, [ApJ](#), 542, 914
Wu, K., & Kiss, L. L. 2008, [A&A](#), 481, 433
Zharikov, S. V., Tovmassian, G. H., & Echevarría, J. 2002, [A&A](#), 390, L23